

Design and simulation of an accelerometer based on NV center spin-strain coupling

Lu-Min Ji(季鲁敏), Li-Ye Zhao(赵立业), and Yu-Hai Wang(王裕海)
Citation: Chin. Phys. B, 2024, 33 (**1**): 017301. DOI: 10.1088/1674-1056/ad09ab
Journal homepage: http://cpb.iphy.ac.cn; http://iopscience.iop.org/cpb

What follows is a list of articles you may be interested in

Lower bound on the spread of valley splitting in Si/SiGe quantum wells induced by atomic rearrangement at the interface

Gang Wang(王刚), Shan Guan(管闪), Zhi-Gang Song(宋志刚), and Jun-Wei Luo(骆军委)
Chin. Phys. B, 2023, 32 (**10**): 107309. DOI: 10.1088/1674-1056/acf208

Strong anharmonicity-assisted low lattice thermal conductivities and high thermoelectric performance in double-anion Mo_2AB_2 (A = S, Se, Te; B=Cl, Br, I) semiconductors

Haijun Liao(廖海俊), Le Huang(黄乐), Xing Xie(谢兴), Huafeng Dong(董华锋), Fugen Wu(吴福根), Zhipeng Sun(孙志鹏), and Jingbo Li(李京波)
Chin. Phys. B, 2023, 32 (**10**): 107304. DOI: 10.1088/1674-1056/ace314

Narrowed $Si_{0.7}Ge_{0.3}$ channel FinFET with subthreshold swing of 64 mV/Dec using cyclic self-limited oxidation and removal process

Hao-Yan Liu(刘昊炎), Yong-Liang Li(李永亮), and Wen-Wu Wang(王文武)
Chin. Phys. B, 2023, 32 (**7**): 077302. DOI: 10.1088/1674-1056/acad71

Machine learning of the Γ-point gap and flat bands of twisted bilayer graphene at arbitrary angles

Xiaoyi Ma(马宵怡), Yufeng Luo(罗宇峰), Mengke Li(李梦可), Wenyan Jiao(焦文艳), Hongmei Yuan(袁红梅), Huijun Liu(刘惠军), and Ying Fang(方颖)
Chin. Phys. B, 2023, 32 (**5**): 057306. DOI: 10.1088/1674-1056/acb2c3

Hexagonal boron phosphide and boron arsenide van der Waals heterostructure as high-efficiency solar cell

Yi Li(李依), Dong Wei(魏东), Gaofu Guo(郭高甫), Gao Zhao(赵高), Yanan Tang(唐亚楠), and Xianqi Dai(戴宪起)
Chin. Phys. B, 2022, 31 (**9**): 097301. DOI: 10.1088/1674-1056/ac6b2a

---

INSTRUMENTATION AND MEASUREMENT

Design and simulation of an accelerometer based on NV center spin–strain coupling

Lu-Min Ji(季鲁敏), Li-Ye Zhao(赵立业)†, and Yu-Hai Wang(王裕海)

Key Laboratory of Micro-Inertial Instrument and Advanced Navigation Technology, Ministry of Education, Department of Instrument Science and Engineering, Southeast University, Nanjing 210096, *China*

(Received 13 September 2023; revised manuscript received 18 October 2023; accepted manuscript online 4 November 2023)

The nitrogen-vacancy (NV) center quantum systems have emerged as versatile tools in the field of precision measurement because of their high sensitivity in spin state detection and miniaturization potential as solid-state platforms. In this paper, an acceleration sensing scheme based on NV spin–strain coupling is proposed, which can effectively eliminate the influence of the stray noise field introduced by traditional mechanical schemes. Through the finite element simulation, it is found that the measurement bandwidth of this ensemble NV spin system ranges from 3 kHz to hundreds of kHz with structure optimization. The required power is at the sub-μW level, corresponding to a noise-limited sensitivity of 6.7×10^{-5} g/$\sqrt{\text{Hz}}$. Compared with other types of accelerometers, this micro-sized diamond sensor proposed here has low power consumption, exquisite sensitivity, and integration potential. This research opens a fresh perspective to realize an accelerometer with appealing comprehensive performance applied in biomechanics and inertial measurement fields.

Keywords: nitrogen-vacancy (NV) accelerometer, spin–strain, diamond

PACS: 73.22.–f, 87.80.Ek, 07.10.Cm, 85.85.+j **DOI:** 10.1088/1674-1056/ad09ab

1. Introduction

From fundamental physics to quantum metrology and quantum information processing, quantum systems have attracted a surge of interest recently.[1–3] Meanwhile, the development of nanofabrication technology has facilitated the fabrication of high-quality mechanical oscillators.[4–6] Benefiting from the diversity of interactions between oscillator motion and quantum systems,[5] quantum hybrid systems (QHSs) with different materials, structures, and principles combining their advantages have been widely explored, including conducting devices, ultracold atoms, and solid-state qubits.[7–12] They have stood out as strong candidates to replace conventional quantum and micro-electromechanical systems (MEMSs) for realizing high-precision magnetic field, acceleration, displacement, and other physical quantity sensing.[13–18]

After studying the influence of strain, electric and magnetic fields on the ground state and excited state of the negatively charged nitrogen-vacancy (NV) center (hereafter referred to as NV center),[19,20] the verification of the NV spin oscillator systems paves the way for its intensive research in the field of precision measurement.[21–24] These QHSs based on NV realize the coupling of spin and mechanical oscillator through magnetic field gradient or the electric field introduced by strain.[22] The mechanical motion provides a coherent control method of the quantum system which in turn can be sensed as a signal source through spin state readout.[5] Owing to the atomic size of the center and the well-established quantum manipulation technology, they have been proven to be a powerful tool to achieve high-resolution measurement of the spin state phase.[25,26] In addition, the high Young's modulus and low internal dissipation of diamond entail the possibility of production of the NV spin-oscillators with high frequency and strength.[5,13,27–29]

However, the field fluctuations induced by the indispensable component including the magnetic tip or the cavity in the NV QHS using magnetic coupling or optical radiation force coupling respectively cannot be ignored.[5,10,27] To obtain systems that are less susceptible to ambient thermal noise and produce fewer stray fields,[23,30,31] researchers have shown a grown emphasis on the NV strain based QHS in which the coupling is intrinsic in the crystal and the simple monolithic structure does not require precise alignment of additional components.[13] University of California Santa Barbara demonstrated that the strain sensitivity of 3×10^{-6} strain/$\sqrt{\text{Hz}}$ and the displacement resolution of 7 nm could be achieved utilizing the designed diamond membrane.[30] University of Basel quantified the NV strain coupling constants and estimated the sensitivity of 76 MHz/μm using their cantilever beam.[32] Australian National University presented a diamond nanopillar structure and optimized the static force sensitivity to 100 pN/$\sqrt{\text{Hz}}$.[33]

So far, previous studies have been conducted to consistently show that the NV strain based QHSs are capable of being burgeoning and leading platforms in the field of metrology, such as vibrometry and pressure sensing. However, what

†Corresponding author. E-mail: liyezhao@seu.edu.cn

© 2024 Chinese Physical Society and IOP Publishing Ltd

is not yet understood is the feasibility of applying NV spin-strain systems to the measurement of acceleration. In this paper, a MEMS accelerometer based on NV strain QHS is proposed. Compared with traditional piezoelectric or capacitive accelerometers, it does not need additional circuit connection and has the advantages of low power consumption, small size, high bandwidth, and satisfactory sensitivity. This research offers a new way of acceleration sensing in biomedicine, vibrometry, and inertial navigation fields.

2. Principle

The acceleration measurement device based on the NV spin-oscillator is shown in Fig. 1(a). The mechanical oscillator fixed at both ends is a diamond membrane containing NV centers. The structural coordinate system (CS) is defined as XYZ, and the view along the Z axis of the structural CS is shown in Fig. 1(b). The total length L, total width W and height D are along the directions of X, Y and Z axes, respectively. The effective sensitive unit is a cuboid in the middle of the whole structure with length L_0 and width W_0. When acceleration as shown is applied along the Z axis direction, the diamond structure generates strain under the action of inertial force.

For this NV spin-strain coupling QHS, the NV electron spin states are initialized by laser pumping at 532 nm with non-radiative transition process and controlled by microwave sequences. The optical readout is realized by the dependence of photoluminescence on spin states. The strain generated by the diamond mechanical oscillator under acceleration changes the intensity and contrast of photoluminescence, thus providing a way to measure the external physical quantity.

The crystal CS is defined as $X_0Y_0Z_0$, and the four NV CSs in the crystal are defined as xyz_m, $m \in \{\mathrm{NV1}, \mathrm{NV2}, \mathrm{NV3}, \mathrm{NV4}\}$. The four internuclear NV axes corresponding to NV1, NV2, NV3, NV4 are along the direction of $[111]$, $[\bar{1}\bar{1}1]$, $[\bar{1}1\bar{1}]$, $[1\bar{1}\bar{1}]$ in the crystal, which are the z axes of the four NV CSs, respectively. The relationship between the crystal CS and the four internal NV CSs is shown in Fig. 2(a). The strain that contributes to atomic displacement and electron density change in the diamond crystal can be regarded as an additional local electric field action on the NV centers. The Hamiltonian can be described by[20,34]

$$\begin{aligned}\frac{H_{\mathrm{NV}}}{h} &= \left(D_0 + d_{\parallel}\varepsilon_{zz}\right) S_z^2 + \gamma \boldsymbol{S}\cdot\boldsymbol{B} \\ &\quad - d_{\perp}\left[\varepsilon_{yy}\left(S_xS_y + S_yS_x\right) + \varepsilon_{xx}\left(S_x^2 - S_y^2\right)\right], \end{aligned} \tag{1}$$

where $D_0 = 2.87$ GHz is the zero field splitting constant. $\gamma = g_{\mathrm{e}}\mu_{\mathrm{B}}/h = 2.8$ MHz/Gs is the electron gyromagnetic ratio. μ_{B} is the Bohr magnet. $g_{\mathrm{e}} = 2.0023$ is the electron g factor. $\boldsymbol{B}$ is the applied magnetic field. S_x, S_y and S_z are the Pauli matrixes of spin 1. The normal strain components in the NV CS are represented by ε_{xx}, ε_{yy} and ε_{zz}. The ground state strain coupling constants parallel to and perpendicular to the NV axis are respectively $d_{\parallel}$ and $d_{\perp}$.[32]

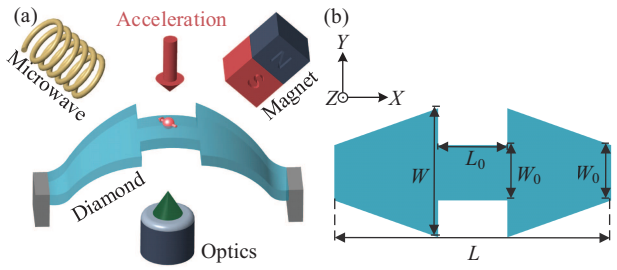


Fig. 1. Diamond-spin-oscillator acceleration sensor: (a) schematic diagram of the overall setup; (b) structure diagram of the diamond mechanical oscillator in structure CS.

Considering that the diamond structure explored here is still a beam with a high aspect ratio, the shear strain components of the structure can be approximately ignored. The optimal lattice cutting direction is selected to minimize the coupling degree between the lateral components of the normal strain and the NV spin. In the NV CS (shown in Fig. 2(b)), the strain $\varepsilon_{\parallel} = \varepsilon_{zz}$ parallel to the NV axis causes the contraction and elongation of the nitrogen bond without changing the C_{3V} symmetry of the NV center, which can be seen as a linear correction to the zero field splitting D_0.[23] The strain $\varepsilon_{\perp} = \sqrt{\varepsilon_{xx}^2 + \varepsilon_{yy}^2}$ perpendicular to the NV axis causes deformation of the carbon bond, destroying the rotational symmetry and breaking the degeneracy of the state $m_{\mathrm{s}} = \pm 1$, resulting in a spin mixing state.[30] The energy level of the NV spin state is presented in Fig. 2(c).

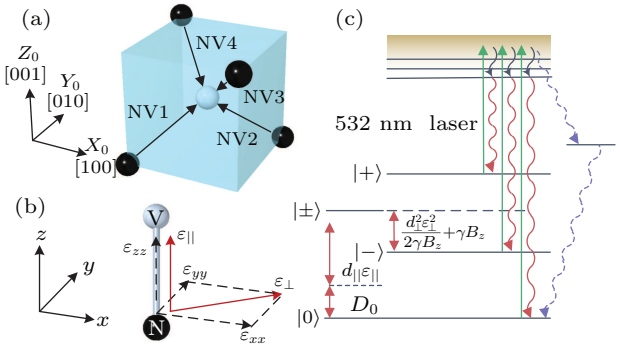


Fig. 2. Schematic diagram of NV spin-strain coupling mechanism. (a) Schematic diagram of the relationship between 4 NV CSs and the crystal CS. (b) Normal strain components in parallel and vertical directions. (c) Energy levels of NV ground state in the presence of strain and magnetic field.

Ramsey sequence can be utilized for acceleration measurement in this scheme. Applying a microwave field with an effective intensity of B_1 and a frequency of $D_0 - \gamma B_z$, the Hamiltonian of the ground spin state under rotating wave approximation is

$$H_{\mathrm{rot}} = h\begin{pmatrix} d_{\parallel}\varepsilon_{zz} + 2\gamma B_z & \frac{\gamma B_1 \mathrm{e}^{-\mathrm{i}\phi}}{2} & -d_{\perp}\left(\varepsilon_{yy} - \mathrm{i}\varepsilon_{xx}\right) \\ \frac{\gamma B_1 \mathrm{e}^{\mathrm{i}\phi}}{2} & 0 & \frac{\gamma B_1 \mathrm{e}^{\mathrm{i}\phi}}{2} \\ -d_{\perp}\left(\varepsilon_{yy} + \mathrm{i}\varepsilon_{xx}\right) & \frac{\gamma B_1 \mathrm{e}^{-\mathrm{i}\phi}}{2} & d_{\parallel}\varepsilon_{zz} \end{pmatrix}. \tag{2}$$

The axial magnetic field B_z is assumed to be large enough to ignore the effect of the lateral strain coupling term $\frac{d_\perp^2 \varepsilon_\perp^2}{2\gamma B_z}$. The subspace of state -1 and state 0 is used as two energy levels approximation. After the evolution process $\pi/2$–τ–$\pi/2$, the two-level system will accumulate phase $\Phi(\tau) = d_\parallel \varepsilon_\parallel \tau$ between the two states. Considering the attenuation caused by the dephasing effect, the probability of the electronic spin state remaining in the state can be expressed as $P(\tau) = \frac{1}{2}[1-\cos(\Phi(\tau))]\exp[-(\frac{\tau}{T_2^*})^n]$, thus the phase information could be obtained through the radiation fluorescence measurement.

Mechanical oscillators can be classified by the geometry of the structure shape and the number of fixed ends. Typical oscillators include singly-clamped structures (e.g., 'U'-shaped and cantilever) and doubly-clamped structures (e.g., bridge).[35] For the general strip diamond structure with double-clamped ends, the vibration of the bridge with a length larger than the cross-section scale can be described by Euler–Bernoulli's theory according to the elastic theory.[29,30] The eigenfrequency can be expressed as

$$\omega_{dn} = \frac{\kappa_n^2}{l^2}\sqrt{\frac{EI}{\rho A}} = \frac{\kappa_n^2 d}{l^2}\sqrt{\frac{E}{12\rho}}, \tag{3}$$

where E is Young's modulus of the material, ρ is the density, A is the cross-section area, l and d are the length and height, respectively. I is the moment of inertia, ω_{dn} is the nth order eigenfrequency, and κ_n is the constant depending on the fixed way and order.[36] As the vibration frequency of the longitudinal mode is much higher than that of the transverse mode, the longitudinal mode is ignored here and only the fundamental mode is analyzed.

3. Simulation results and analysis

3.1. Sensitivity analysis

Assuming that the NV axial strain of the diamond mechanical oscillator caused by the external acceleration a is $\varepsilon_\parallel$, the scale factor determined by the diamond structure and cutting orientation can be expressed as $\varepsilon_\parallel/a$. Considering that the interrogation time determined by the quantum manipulation sequence is τ, for the Ramsey and spin echo sequences, τ can be taken as the dephasing time and coherence time, i.e., $\tau \le T_2^*$ and $\tau \le T_2$. A general sensitivity expression for the acceleration measurement can be obtained, $S_a \propto \left(\frac{\varepsilon_\parallel}{a}\right)^{-1}\frac{1}{\sqrt{\tau}}$. In addition, the sensitivity of an NV spin-strain QHS is related to spin projection noise, photon shot noise, and overhead time.[37] Therefore, for the system here using Ramsey sequences, the noise determined acceleration sensing sensitivity can be expressed as follows:

$$S_\varepsilon = \left(\frac{\varepsilon_\parallel}{\Delta a}\right)^{-1}\frac{e^{\left(\frac{\tau}{T_2^*}\right)^p}}{2\pi d_\parallel C\sqrt{N}\sqrt{\tau}}\sqrt{\frac{\tau+t_{\rm pol}+t_{\rm ro}}{\tau}}, \tag{4}$$

where C is the fluorescence collection efficiency $C = 0.3$.[38] p can be 1, 2, 3, and $p = 2$ is taken here. $t_{\rm pol}$ and $t_{\rm ro}$ are the initialization time and readout time, respectively, which can be ignored. Therefore, τ is taken as $\tau = T_2^*/2$ to obtain the optimal sensitivity. The number of effective spins is taken as a quarter of the total number of centers $N = nV/4$. The nitrogen density is about 10^{18} cm^{-3}, thus the NV center density is $n = 10^{17}$ cm^{-3} with NV center conversion ratio 0.1.[38] T_2^* is taken as 10 μs, V is the effective sensing volume, $d_\parallel$ is taken as 13.3 GHz.[33] Therefore, the sensitivity of acceleration measurement is expressed as

$$S_\varepsilon = \left(\frac{\varepsilon_\parallel}{a}\right)^{-1}\frac{\sqrt{2}e^{\left(\frac{1}{2}\right)^2}}{\pi d_\parallel C\sqrt{nV}\sqrt{T_2^*}}. \tag{5}$$

3.2. Optimization of diamond crystal cutting orientation

The structural strain tensor needs to be converted into the NV CSs to calculate the effective strain. Therefore, the cutting direction of the diamond crystal is optimized to reduce the coupling of transverse strain with the NV axis. The X axis in the structure CS can be chosen to be along [100], [110] or [111] direction with a great degree of symmetry in the crystal,[39] which is denoted as XYZ_k $k \in \{1,2,3\}$ corresponding to the above three cases. Without loss of generality, the orientations of the three structure CSs XYZ_k and the four NV CSs xyz_m in the crystal CS are assumed in Table 1. According to the rotation matrix $\boldsymbol{L}_k^m$ of the kth structure CS to the mth NV CS, the strain tensor $\varepsilon_{xyzm} = \boldsymbol{L}\varepsilon_{XYZ}\boldsymbol{L}^{\rm T}$ in the NV CS can be obtained. The strain tensor forms in the structure CS and the NV CS are respectively shown below:

$$\varepsilon_{XYZ} = \begin{bmatrix} \varepsilon_{XX} & \varepsilon_{XY} & \varepsilon_{XZ} \\ \varepsilon_{YX} & \varepsilon_{YY} & \varepsilon_{YZ} \\ \varepsilon_{ZX} & \varepsilon_{ZY} & \varepsilon_{ZZ} \end{bmatrix}, \tag{6}$$

$$\varepsilon_{xyzm} = \begin{bmatrix} \varepsilon_{xx} & \varepsilon_{xy} & \varepsilon_{xz} \\ \varepsilon_{yx} & \varepsilon_{yy} & \varepsilon_{yz} \\ \varepsilon_{zx} & \varepsilon_{zy} & \varepsilon_{zz} \end{bmatrix}. \tag{7}$$

The strain components in the corresponding CS satisfy $\varepsilon_{ij} = \varepsilon_{ji}$, $i, j \in \{X,Y,Z\}$, $i \ne j$ and $\varepsilon_{pq} = \varepsilon_{qp}$, $pq \in \{x,y,z\}$, $p \ne q$.

Table 1. Representation of 3 structure CSs and 4 NV CSs in the crystal CS.

CSs		X or $x\parallel$	Y or $y\parallel$	Z or $z\parallel$
Structure CS	XYZ_1	[100]	[010]	[001]
	XYZ_2	[110]	[$\bar{1}$10]	[001]
	XYZ_3	[111]	[$\bar{1}$10]	[$\bar{1}\bar{1}$2]
NV CS	$xyz_{\rm NV1}$	[$\bar{1}$10]	[$\bar{1}\bar{1}$2]	[111]
	$xyz_{\rm NV2}$	[1$\bar{1}$0]	[112]	[$\bar{1}\bar{1}$1]
	$xyz_{\rm NV3}$	[110]	[1$\bar{1}\bar{2}$]	[$\bar{1}$1$\bar{1}$]
	$xyz_{\rm NV4}$	[$\bar{1}$1$\bar{0}$]	[$\bar{1}$1$\bar{2}$]	[1$\bar{1}\bar{1}$]

A finite element analysis software is used to obtain the strain distribution of the diamond structure under the action of acceleration along the $-Z$ axis. Poisson ratio, Young's modulus, and density of diamond are 0.069, 1220 GPa, and

3.515 g/cm^3, respectively.[33,36] In Figs. 3(a)–3(c), the strain is concentrated at the sensitive unit and the fixed ends of the overall structure. In the length direction of the oscillator (X axis in the structure CS), the strain at the sensitive unit is relatively high. In the height direction (Z axis), the strain at the sensitive element gradually decreases from the surface to the middle. It is apparent from Fig. 3(d) that in the sensitive unit, ε_{XZ} and ε_{YZ} are significantly smaller among the shear components of the strain tensor, and about one order of magnitude lower than ε_{XY}. Similarly, ε_{XX} is the maximum among the normal strain, one order of magnitude higher than ε_{XX} and ε_{YY}. This result can be explained by the fact that the structure is overall beam-shaped and the acceleration is input along the Z direction. Meanwhile, the shear strain components, which can be ignored, are more than two orders of magnitude lower than the normal strain components.

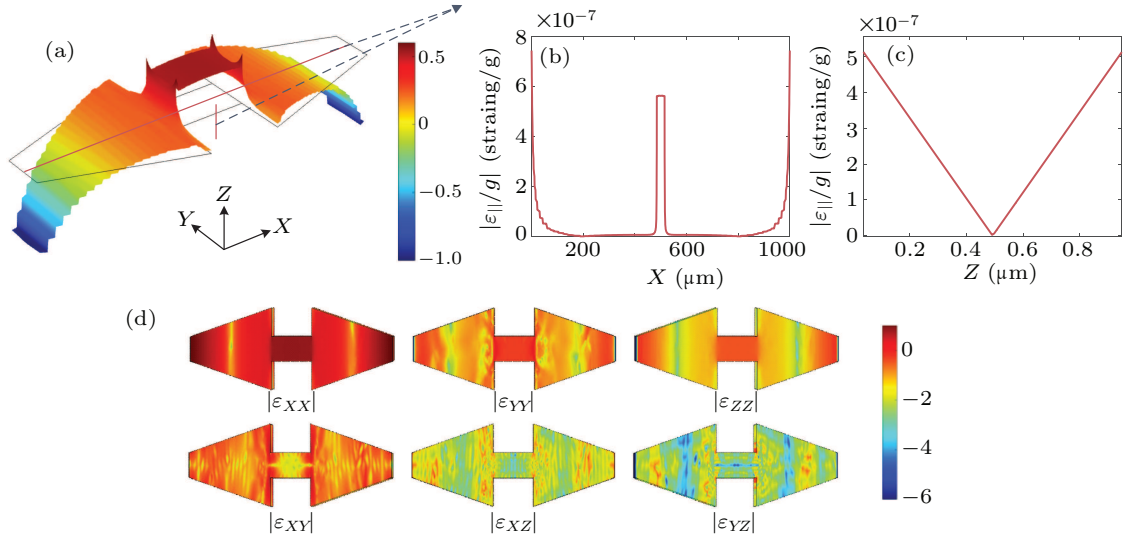


Fig. 3. Mechanical simulation of the spin–strain coupling oscillator. (a) The log-normalized effective strain distribution of the diamond structure on the surface parallel to the XOY plane under acceleration. The effective strain distribution along the length (b) and height (c) directions of the structure is shown in (a). (d) Schematic diagram of the components of the log-normalized strain on the surface of the structure parallel to the plane XOY.

The influence of different diamond cutting orientations on the sensing performance can be analyzed according to the above simulation results. The effective strain transformation results are calculated for three different diamond cut orientations in four NV CSs shown in Table 1. The effective strain components $\varepsilon_{\parallel}$ are present in Table 2. Considering that the influence of the normal strain components perpendicular to the NV axis on the energy splitting between 0 and 1 states can be approximated as $d_{\perp}^2((\varepsilon_{xxm})^2+(\varepsilon_{yym})^2)/(2\gamma B)$ according to Eq. (6), we can ignore the normal strain component $\varepsilon_{\perp}$ and shear strain in the NV CS, and take $\varepsilon_{\parallel}$ as the effective strain. For the normalization of the normal strain tensor of the structure, ε_{XX}, ε_{YY} and ε_{ZZ} can be expressed as 1, 0.1, 0.1. It can be concluded that the X axis along [110] or [111] could achieve a 19.3% improvement of the effective strain than being along [100] direction. In addition, the effective strain of NV1 and NV2 is equal, which increases the number of the effective NV centers twice and optimizes the sensitivity of the ensemble NV measurement scheme of acceleration by $\sqrt{2}$ times. The results of this investigation show that the [110] direction is better because there is no energy level difference in this direction NV3 and NV4, so the energy level splitting can be easier to identify.

Table 1. Normal strain component parallel to the NV axis in the NV CS.

	$X \parallel [100]$	$X \parallel [110]$	$X \parallel [111]$
NV1	$0.83\varepsilon_{XX}+0.53\varepsilon_{XY}-0.53\varepsilon_{XZ}+0.083\varepsilon_{YY}-0.17\varepsilon_{YZ}+0.083\varepsilon_{ZZ}$	ε_{XX}	ε_{XX}
NV2	$0.83\varepsilon_{XX}-0.53\varepsilon_{XY}-0.53\varepsilon_{XZ}+0.083\varepsilon_{YY}+0.17\varepsilon_{YZ}+0.083\varepsilon_{ZZ}$	ε_{XX}	ε_{XX}
NV3	$0.83\varepsilon_{XX}+0.53\varepsilon_{XY}+0.53\varepsilon_{XZ}+0.083\varepsilon_{YY}+0.17\varepsilon_{YZ}+0.083\varepsilon_{ZZ}$	$0.67\varepsilon_{XX}+0.94\varepsilon_{XZ}+0.33\varepsilon_{ZZ}$	$0.67\varepsilon_{XX}+0.54\varepsilon_{XY}+0.77\varepsilon_{XZ}+0.11\varepsilon_{YY}+0.31\varepsilon_{YZ}+0.22\varepsilon_{ZZ}$
NV4	$0.83\varepsilon_{XX}-0.53\varepsilon_{XY}+0.53\varepsilon_{XZ}+0.083\varepsilon_{YY}-0.17\varepsilon_{YZ}+0.083\varepsilon_{ZZ}$	$0.67\varepsilon_{XX}+0.94\varepsilon_{XZ}+0.33\varepsilon_{ZZ}$	$0.67\varepsilon_{XX}-0.54\varepsilon_{XY}+0.77\varepsilon_{XZ}+0.11\varepsilon_{YY}-0.31\varepsilon_{YZ}+0.22\varepsilon_{ZZ}$

3.3. Structural parameters influence on sensing performance

To characterize the sensing performance of the spin-strain coupling system, simulations are conducted from the perspectives of sensitivity, power, and size. Based on the analysis above, the diamond cutting orientation $X \parallel [110]$ and effective NV axis of NV1 and NV2 are applied in the simulation, with the corresponding effective strain $\varepsilon_{\parallel}=\varepsilon_{XX}$.

First of all, the influence of the sensitive unit size on the sensitivity is simulated when the overall size of the structure is determined. We choose $L = 1000$ μm, $W = 100$ μm, $D = 1$ μm, and length-height ratio to be 1000.[40] The single NV center is in the center of the sensitive unit surface to avoid strain upheaval points for a single NV scheme. For the ensemble NV scheme, the effective center is taken as the whole sensitive unit containing centers. The length L_0 and width W_0 are adjusted with the optimization principle: $D \le L_0 \le L$, $D \le W_0 \le W$. So the variation ranges of L_0 and W_0 are respectively [1 μm, 1000 μm] and [1 μm, 100 μm].

The results of sensitivity change with the size of the sensitive unit are shown in Figs. 4(a) and 4(b). Points A, marked with circles, and points B, marked with asterisks, indicate the best and worst sensitivity simulation results, respectively. Evidently, the sensitivity of the ensemble NV center-based system is considerably better than that of the single NV center-based system. Optimal sensitivities are 6.7×10^{-5} g/$\sqrt{\text{Hz}}$ ($L_0 = 30$ μm, $W_0 = 1$ μm) and 0.068 g/$\sqrt{\text{Hz}}$ ($L_0 = 1$ μm, $W_0 = 1$ μm), respectively. If the length and width of the sensitive unit are equal to the length and width of the overall structure, respectively, the structure is a simple Euler–Bernoulli beam. The corresponding sensitivity and power consumption are not optimal, which verifies the effectiveness of the proposed structure in this work. In addition, the obvious difference between the two measurement methods is that for the multi-spin scheme, the structural parameters leading to relatively good performance correspond to the length and width of the sensitive element being synchronous large and small. While for the single-spin scheme, they only correspond to the length and width being small at the same time. Reducing the overall size of the sensitive unit can increase the effective mass and decrease the system's stiffness for both single and ensemble center based schemes. When the length and width are increasing simultaneously, the sensitivity is excellent for the muti-spin scheme, which benefits from the increase in the number of effective NV centers. Through this structure optimization, the sensitivity of the single spin and multi-spin measurement schemes can be respectively improved by 2.4 and 1.6 orders of magnitude.

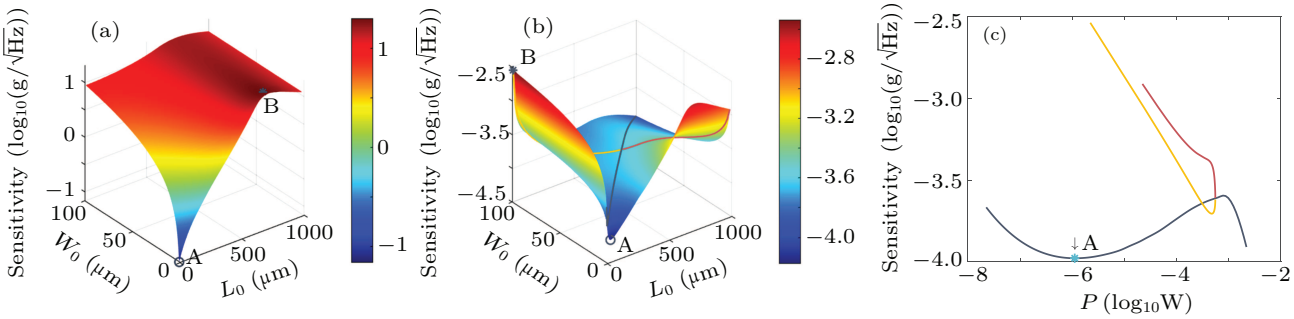


Fig. 4. The comprehensive effect of the length and width of the sensitive unit in (a) single NV and (b) ensemble NV center based schemes on the sensitivity of acceleration measurement. Points A and B represent the best and worst simulation results in both figures. (c) The influence of excited light power on the sensitivity of the ensemble NV center based sensor. Point A represents the best simulation result.

Considering that the sensitivity optimization procedures for a multi-spin system have different requirements on the excitation light power, we analyze the effect of laser power on the sensitivity of acceleration measurements later. The black line through $(L_{0\min}, W_{0\min})$ and $(L_{0\max}, W_{0\max})$, the red line through $(L_{0\max}, W_{0\min})$ and $(L_{0\max}/2, W_{0\max}/2)$, the yellow line through $(L_{0\min}, W_{0\max})$ and $(L_{0\max}/2, W_{0\max}/2)$ in Fig. 4(a) are chosen to calculate the power consumption. Assume that each NV center requires three excited photons of 532 nm to achieve optical polarization, then the laser power expression is

$$P = \frac{6Nhc}{T_2^* \lambda}, \tag{8}$$

where h is Planck's constant, c is the speed of light, and the 532 nm light wavelength λ is taken. As can be seen from the black curve in Fig. 4(c), with the increase of the available power, the curve shows a trend of decreasing, increasing, and then decreasing. This phenomenon can be attributed to the counterbalance between the system response and the effective color number. When the length and width of the sensitive unit vary by the same multiple, the system performance is optimized at a certain intermediate value, as indicated by point A marked with a circle. The corresponding moderate power is only 1.1 μW, which is three orders of magnitude less than the maximum power, and better sensitivity can be obtained. It can be concluded from the red and yellow lines in Fig. 4(c) that the sensitivity nearly shows a monotonically improving trend with the increase of provided power. Starting from that point, the sensitivity of increasing the length is slightly better than that of increasing the width with a fixed power consumption. Moreover, for the optimal sensitivity of the multi-spin scheme aforementioned, the power required is only 0.69 μW, on the sub-μW scale.

Then we explore the influence of the structure height D on sensitivity, and set $W = 1000$ μm, $L = 100$ μm, $L_0 = W_0 = 10$ μm, 1 μm $< D <$ 10 μm. As shown in Fig. 5, the sensitivity improvement is less than one order magnitude (about 3 times)

when the height changes by 10 times, indicating that the thickness has a limited effect on the performance under the current parameters.

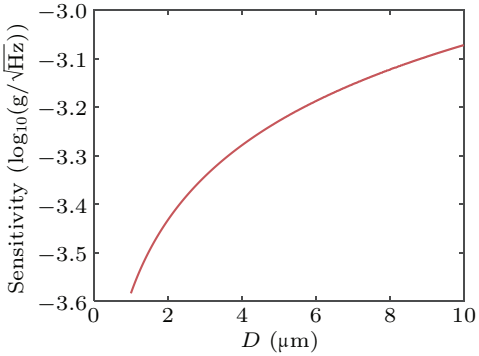


Fig. 5. The influence of the overall structure height on the sensitivity.

Finally, the frequency response caused by the change in the overall length of the structure with other parameters being constant ($W = 100$ μm, $L_0 = 30$ μm, $W_0 = 1$ μm, and $D = 1$ μm) is investigated. As shown in Fig. 6(a), if the length L increases from 100 μm to 1000 μm, the corresponding resonant frequency will decrease from the order of 1 MHz to the order of 10 kHz. It can be inferred from the inset of Fig. 6(b) that the eigenfrequency of the system and the total length L are negatively correlated, and can be fitted by $y = 5.03 \times 10^6/x^{1.97}$. This relationship, which is approximately $w_1 \propto 1/L^2$, is similar to that of the Eulbernoulli beam.

What's more, the relationship between the sensitivity and the bandwidth is simulated in Fig. 6(b). When the length is increased by one order of magnitude, the corresponding bandwidth, from 790 kHz to 10 kHz, is decreased by nearly two orders of magnitude, and the sensitivity is improved by nearly three orders of magnitude. The simulation result represents a trade-off between bandwidth and sensitivity. For the frequency of acceleration lower than 3 kHz, a better sensitivity can be obtained when L is chosen to be sufficiently large, e.g., 1000 μm. For a high-frequency signal (hundreds of kHz) sensing, a smaller L is preferred to obtain a larger working range.

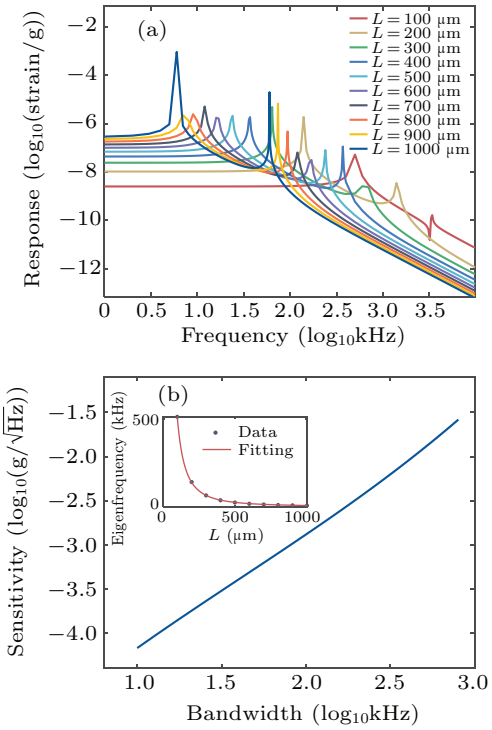


Fig. 6. Influence of different overall lengths L on sensor performance. (a) Different frequency responses of effective strain. (b) The relationship between bandwidth and sensitivity. The inset shows the impact of L on the eigenfrequency.

4. Discussion

The performance compared with other types of MEMS accelerometers is shown in Table 3. Compared with traditional accelerometers, the superiority of the MEMS accelerometer proposed in this paper is reflected in its flexibility, versatility, and integrated potential. With its fine sensitivity, wide bandwidth, and non-contact measurement properties, this sensor has broad prospects in inertial navigation,[41] seismology, and bioscience in the future.

Table 3. Main performance comparisons of this work and other MEMS accelerometers.

Classification	Capacitive[42]	Capacitive[43]	Resonant[44]	This work
Principles	acceleration-capacitance	acceleration-capacitance	acceleration-frequency	acceleration-fluorescence
Sensitivity (μg/$\sqrt{Hz}$)	2	380	2	67
Power consumption	3.6 mW	1.4 mW	583 μW	0.69 μW
Bandwidth	200 Hz		> 200 Hz	> 3 kHz

In general, although the NV strain based system does not require the precise alignment of spin and oscillator, the precise positioning of the NV center in the single NV center scheme is necessary, which is still challenging. This problem can be weakened by using the ensemble NV system. However, the noise calculation method described here, which does not fully consider the impact of impurities in ensemble samples, cannot be ignored in practical application.[5] To further improve sensor performance, optimization could be conducted from the following perspectives in the future. The Ramsey sequence could be replaced with spin echo with longer interrogation time to improve the sensitivity by about $\sqrt{T_2/T_2^*}$ times. Similarly, a more complex dynamic decoupling sequence can further increase the interrogation time at the cost of bandwidth loss.[38,45] Considering the sensitivity of the ensemble NV based system related to the number of effective NV centers,

a scheme with an array of small-volume diamond oscillators could be investigated with the development of nanoelectromechanical systems (NEMS) fabrication technology. The method of coupling the oscillator with the NV spin excited state to improve the coupling strength is also worth further exploring.[36]

5. Conclusion

In summary, this work proposes a diamond based spin-strain coupling scheme for acceleration measurement and characterizes its performance. The effective strain under acceleration applied along three symmetrical crystal directions is analyzed through the transformation between the structure, crystal, and NV CSs. The measurement bandwidth ranges from 3 kHz to hundreds of kHz with structure optimization. The sensitivity can reach 6.7×10^{-5} g/$\sqrt{\text{Hz}}$ with μm level effective size and sub-μW power consumption.

Acknowledgements

Project supported by the National Natural Science Foundation of China (Grant No. 62071118) and the Primary Research & Development Plan of Jiangsu Province (Grant No. BE2021004-3).

References

[1] Rajendran S, Zobrist N, Sushkov A O, Walsworth R and Lukin M 2017 *Phys. Rev. D* **96** 035009
[2] Jarmola A, Lourette S, Acosta V M, Birdwell A G, Blümler P, Budker D, Ivanov T and Malinovsky V S 2021 *Sci. Adv.* **7** 1
[3] Degen C L, Reinhard F and Cappellaro P 2017 *Rev. Mod. Phys.* **89** 035002
[4] Rath P, Khasminskaya S, Nebel C, Wild C and Pernice W H P 2013 *Nat. Commun.* **4** 1690
[5] Lee D, Lee K W, Cady J V, Ovartchaiyapong P and Jayich A C B B 2017 *J. Opt.* **19** 033001
[6] Adiga V P, Sumant A V, Suresh S, Gudeman C, Auciello O, Carlisle J A and Carpick R W 2009 *Phys. Rev. B* **79** 245403
[7] Etaki S, Poot M, Mahboob I, Onomitsu K, Yamaguchi H and Van Der Zant H S J 2008 *Nat. Phys.* **4** 785
[8] Pirkkalainen J M, Cho S U, Li J, Paraoanu G S, Hakonen P J and Sillanpää M A 2012 *Nature* **494** 211
[9] Jöckel A, Faber A, Kampschulte T, Korppi M, Rakher M T and Treutlein P 2015 *Nat. Nanotechnol.* **10** 55
[10] Camerer S, Korppi M, Jöckel A, Hunger D, Hänsch T W and Treutlein P 2011 *Phys. Rev. Lett.* **107** 223001
[11] Arcizet O, Jacques V, Siria A, Poncharal P, Vincent P and Seidelin S 2011 *Nat. Phys.* **7** 879
[12] Kolkowitz S, Bleszynski Jayich A C, Unterreithmeier Q P, Bennett S D, Rabl P, Harris J G E and Lukin M D 2012 *Science* **335** 1603
[13] Barfuss A, Kasperczyk M, Kölbl J and Maletinsky P 2019 *Phys. Rev. B* **99** 174102
[14] Kumar P and Bhattacharya M 2017 *Frontiers in Optics* 2017 p. FTh3B.2
[15] Chen X Y Y and Yin Z Q Q 2018 *Opt. Express* **26** 31577
[16] Xiao K W, Zhou L M, Yin Z Q and Zhao N 2018 *Commun. Theor. Phys.* **70** 97
[17] Be'Er O, Ohadi H, Del Valle-Inclan Redondo Y, Ramsay A J, Tsintzos S I, Hatzopoulos Z, Savvidis P G and Baumberg J J 2017 *Appl. Phys. Lett.* **111** 261104
[18] Bai R, Zhu X, Yang F, Gao T, Wang Z, Yu L, Wang J, Zhou L and Du G 2022 *Chin. Phys. B* **31** 074203
[19] Dolde F, Fedder H, Doherty M W, Nöbauer T, Rempp F, Balasubramanian G, Wolf T, Reinhard F, Hollenberg L C L, Jelezko F and Wrachtrup J 2011 *Nat. Phys.* **7** 459
[20] Doherty M W, Dolde F, Fedder H, Jelezko F, Wrachtrup J, Manson N B and Hollenberg L C L 2012 *Phys. Rev. B* **85** 205203
[21] Doherty M W, Manson N B, Delaney P, Jelezko F, Wrachtrup J and Hollenberg L C L 2013 *Phys. Rep.* **528** 1
[22] Zhangqi Y I N, Nan Z, Tongcang L I, Yin Z, Zhao N and Li T 2015 *Sci. China Phys. Mech. Astron.* **58** 1
[23] Meesala S, Sohn Y I, Atikian H A, Kim S, Burek M J, Choy J T and Lončar M 2016 *Phys. Rev. Appl.* **5** 034010
[24] Lee K W, Lee D, Ovartchaiyapong P, Minguzzi J, Maze J R and Bleszynski Jayich A C 2016 *Phys. Rev. Appl.* **6** 034005
[25] Broadway D A, Johnson B C, Barson M S J, Lillie S E, Dontschuk N, McCloskey D J, Tsai A, Teraji T, Simpson D A, Stacey A, McCallum J C, Bradby J E, Doherty M W, Hollenberg L C L and Tetienne J P 2019 *Nano Lett.* **19** 4543
[26] Shandilya P K, Flagan S, Carvalho N C, Zohari E, Kavatamane V K, Losby J E and Barclay P E 2022 *J. Light. Technol.* **40** 7538
[27] Burek M J, Ramos D, Patel P, Frank I W and Lončar M 2013 *Appl. Phys. Lett.* **103** 131904
[28] Kara V, Sohn Y I, Atikian H, Yakhot V, Lončar M and Ekinci K L 2015 *Nano Lett.* **15** 8070
[29] Heidrich N, Iankov D, Hees J, Pletschen W, Sah R E, Kirste L, Zuerbig V, Nebel C, Ambacher O and Lebedev V 2013 *J. Micromechanics Microengineering* **23** 125017
[30] Ovartchaiyapong P, Lee K W, Myers B A and Jayich A C B 2014 *Nat. Commun.* **5** 4429
[31] Barfuss A, Teissier J, Neu E, Nunnenkamp A and Maletinsky P 2015 *Nat. Phys.* **11** 820
[32] Teissier J, Barfuss A, Appel P, Neu E and Maletinsky P 2014 *Phys. Rev. Lett.* **113** 020503
[33] Barson M S J, Peddibhotla P, Ovartchaiyapong P, Ganesan K, Taylor R L, Gebert M, Mielens Z, Koslowski B, Simpson D A, McGuinness L P, McCallum J, Prawer S, Onoda S, Ohshima T, Bleszynski Jayich A C, Jelezko F, Manson N B and Doherty M W 2017 *Nano Lett.* **17** 1496
[34] Bennett S D, Yao N Y, Otterbach J, Zoller P, Rabl P and Lukin M D 2013 *Phys. Rev. Lett.* **110** 156402
[35] Brueckner K, Niebelschuetz F, Tonisch K, Foerster C, Cimalla V, Stephan R, Pezoldt J, Stauden T, Ambacher O and Hein M A 2011 *Phys. Status Solidi Appl. Mater. Sci.* **208** 357
[36] MacQuarrie E R, Otten M, Gray S K and Fuchs G D 2017 *Nat. Commun.* **8** 14358
[37] Barry J F, Schloss J M, Bauch E, Turner M J, Hart C A, Pham L M and Walsworth R L 2020 *Rev. Mod. Phys.* **92** 15004
[38] Taylor J M, Cappellaro P, Childress L, Jiang L, Budker D, Hemmer P R, Yacoby A, Walsworth R and Lukin M D 2008 *Nat. Phys.* **4** 810
[39] Klein C A and Cardinale G F 1993 *Diam. Relat. Mater.* **2** 918
[40] Ali Momenzadeh S, de Oliveira F F, Neumann P, Bhaktavatsala Rao D D, Denisenko A, Amjadi M, Chu Z, Yang S, Manson N B, Doherty M W and Wrachtrup J 2016 *Phys. Rev. Appl.* **6** 024026
[41] Zhang J Y, Chen L L, Cheng Y, Luo Q, Shu Y B, Duan X C, Zhou M K and Hu Z K 2020 *Chin. Phys. B* **29** 093702
[42] Yücetaş M, Pulkkinen M, Kalanti A, Salomaa J, Aaltonen L and Halonen K 2012 *IEEE J. Solid-State Circuits* **47** 1721
[43] Petkov V P, Balachandran G K and Beintner J 2014 *IEEE J. Solid-State Circuits* **49** 262
[44] Zhao Y, Zhao J, Wang X, Xia G M, Qiu A P, Su Y and Xu Y P 2015 *IEEE J. Solid-State Circuits* **50** 2113
[45] Bar-Gill N, Pham L M, Jarmola A, Budker D and Walsworth R L 2013 *Nat. Commun.* **4** 1743